

Slurry extrusion on Ceres from a convective mud-bearing mantle

Ottaviano Ruesch^{1*}, Antonio Genova^{2,8}, Wladimir Neumann^{3,4}, Lynnae C. Quick⁵, Julie C. Castillo-Rogez⁶, Carol A. Raymond⁶, Christopher T. Russell⁷ and Maria T. Zuber^{1b}

Ceres is a 940-km-diameter dwarf planet that is predominantly composed of silicates and water ice. In Ceres' partially differentiated interior, extrusive processes have led to the emplacement on its surface of domes with heights of kilometres. Here we report the analysis of a gravity anomaly detected by the Dawn spacecraft, which is associated with the geologically recent dome Ahuna Mons. By modelling the anomaly with a mass concentration method, we determine that the subsurface structure includes a regional mantle uplift, which we interpret as a plume. This structure is the probable source of fluids forming Ahuna Mons and, together with constraints from the dome's morphology, indicates a rheological regime corresponding to a slurry of brine and solid particles. We propose that the properties of such a solid-liquid mixture can explain the viscous relaxation and the mineralogy of the dome. The presence of a plume and of slurry material indicate recent convection in a mud-bearing mantle. The inferred slurry extrusion on Ceres differs from the water-dominated cryovolcanism of icy satellites, and so reveals compositional and rheological diversity in extrusive phenomena on planetary surfaces.

Ceres is the largest body in the asteroid belt, with a bulk density of $2,162 \text{ kg m}^{-3}$ (ref. ¹). It is a water-ice-rich protoplanet that experienced aqueous alteration in its past². Between 2015 and 2018, the Dawn spacecraft performed a reconnaissance orbital mission of the dwarf planet. One of the primary mission goals was to characterize the extent of Ceres' internal differentiation by determining its surface and interior properties². The clear identification of a centrally condensed mass implies partial differentiation of the dwarf planet^{3–6}. Global-scale topography analysis suggested that the upper part of the mantle, below an approximately 40 km thick crust, has a relatively low viscosity, consistent with liquid pore fluids⁷, while leaving unknown the nature and dynamics of the mantle, as well as the potential link to its surface expression.

Stereo imaging⁸ with Dawn's Framing Camera enabled the reconstruction of the global shape, revealing a prominent topographic dome (~4 km high and 17 km wide), named Ahuna Mons⁹. The morphology and morphometry of the dome indicate an extrusive formation mechanism involving fluid-bearing (volcanic) material, and thus an unambiguously endogenic process⁹. This origin is supported by its composition, rich in sodium carbonate, the solid residue of a brine¹⁰. The construction of the dome is consequently related to the properties of the subsurface and, ultimately, to the extent of differentiation of Ceres. To study the interior structure of the dwarf planet, Dawn performed a gravity science investigation of a year and half of X-band radio tracking data and surface optical landmarks from the Dawn spacecraft⁴. The gravity field is represented in spherical harmonic coefficients to degree and order 18 (Ceres18C) with an accuracy of about 10 mGal at the equator, which consider the full covariance matrix⁴. The low gravity to topography admittance^{3–5}, corroborated by rheological constraints from finite-element geodynamical simulations⁷, indicates that Ceres' subsurface

is consistent with Airy isostatic compensation, in which large-scale topographic relief is supported by variations at the crust–mantle boundary. Under this assumption, the interior structure that best satisfies the observational geodetic constraints with a two-layer (crust and mantle) model is characterized by a crustal density $\rho_c = 1,287 \text{ kg m}^{-3}$, a mean crustal thickness of 41 km and a mantle density $\rho_m = 2,434 \text{ kg m}^{-3}$ (Methods)^{4,5}. To characterize the subsurface beneath Ahuna Mons we perform a gravity analysis using this two-layer structure.

Gravity isostatic anomaly analysis. After subtracting the gravity contribution of the topographic load and the isostatic compensation at the crust–mantle boundary from the Ceres18C gravity field (Methods), an approximately 50–60 mGal strong positive isostatic anomaly remains, associated with Ahuna Mons and its surroundings (Fig. 1), as previously noticed^{5,11}.

To characterize the origin of the mass concentration (mascon) that is responsible for the positive isostatic anomaly, we used a Markov-chain Monte Carlo (MCMC) technique that selects the properties of a three-dimensional ellipsoidal mascon, which yields gravity anomalies consistent with the measurements. The adjusted mascon parameters are density ($\Delta\rho = \rho_M - \rho_c$), principal axes a , b and c and depth (h) below the dome, as well as its geographic location and orientation (Methods). The parameters are determined non-uniquely by minimizing the anomaly between the modelled mascon gravity and the gravity derived by Dawn. The task is performed by exploiting the two-dimensional gravity anomaly map in the region of interest, using a projection on a sphere, and not solely one-dimensional profiles. Interior model solutions that result from gravity anomaly analysis are intrinsically non-unique and, as a consequence, our method is applied with the following conditions:

¹European Space Agency, European Space and Technology Center, Noordwijk, The Netherlands. ²Department of Earth, Atmospheric and Planetary Sciences, Massachusetts Institute of Technology, Cambridge, MA, USA. ³Institut für Planetologie, University of Münster, Münster, Germany.

⁴Institut für Planetenforschung, Deutsches Zentrum für Luft- und Raumfahrt, Berlin, Germany. ⁵Center for Earth and Planetary Studies, National Air and Space Museum, Smithsonian Institution, Washington, DC, USA. ⁶Jet Propulsion Laboratory, California Institute of Technology, Pasadena, CA, USA.

⁷Department of Earth, Planetary and Space Sciences, University of California, Los Angeles, CA, USA. ⁸Present address: Sapienza Università di Roma, Rome, Italy. *e-mail: ottaviano.ruesch@esa.int

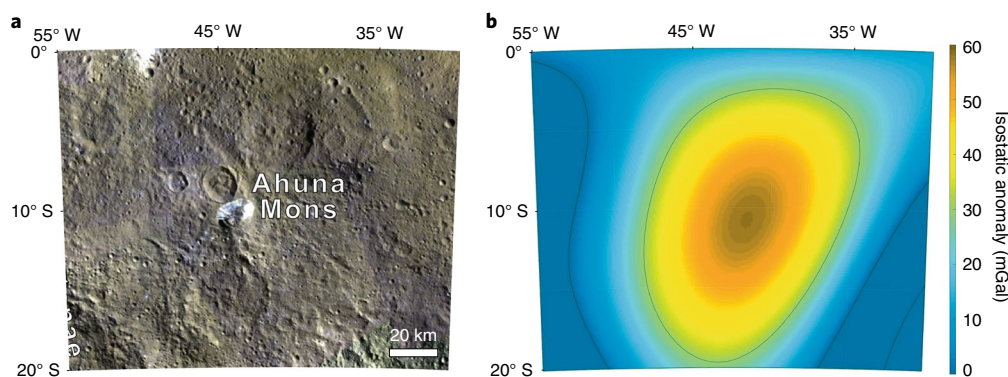


Fig. 1 | Colocation of volcanic dome and isostatic gravity anomaly. **a**, A false-colour mosaic (R, 0.97 μm ; G, 0.75 μm ; B, 0.44 μm) of the region of Ahuna Mons from Dawn Framing Camera observations. The dome of Ahuna Mons is close to the centre of the mosaic, and its high-reflectance areas are steep flanks rich in carbonates and phyllosilicates¹⁰. **b**, The isostatic anomaly represented with spherical harmonic degrees $l=5\text{--}14$ and showing about 50–60 mGal at approximately the same coordinates as Ahuna Mons for the same area as **a**.

the mascon is assumed to be within the crust and have a density lower than the mantle density. This first condition is set by the requirements of the canonical isostatic correction because isostatic anomalies reflect density variations solely in the crust. The second assumption derives from the physical instability of a mascon with density higher than the mantle¹² and from Ceres' geophysical limitations to produce a concentration of high-density mineral species away from the body's centre of mass^{4,13}. Other shapes of the mascon were tested and produced larger residuals than did an ellipsoidal shape. We note that the derived properties described below are based on the assumptions of an ellipsoidal shape of the mascon and an absence of density variations within it.

A mantle uplift beneath Ahuna Mons. The results of our investigation match the observed anomaly with an uncertainty of about 6 mGal, which is fully consistent with the formal errors of Ceres18C in that region of the dwarf planet (Fig. 2). Two distinctive mascon configurations emerge from the final ensemble of solutions (Fig. 3) (Methods).

In the most probable scenario ($\sim 305,000$ models, Fig. 2b), the majority of MCMC models (70%) have a mascon density in the range of 2,300–2,400 kg m^{-3} , close to the mean density of the mantle. The same percentage of models have the base of the mascon within 700 m of the crust–mantle interface. The shapes of the models' ellipsoids are oblate with semimajor axes of Gaussian distributions $a=39\pm 2$ km, $b=22\pm 3$ km and $c=5\pm 1$ km, centred at $h=36\pm 1$ km. The horizontal dimensions of the mascon are similar to the horizontal resolution of the gravity field and indicate that the gravity field resolution limits the determination of mascon horizontal size. An analysis using a gravity field at higher spatial resolution with spherical harmonic degrees up to 16, however, reveals only a change in the horizontal tilt angle. Vertical axis and density contrast are not affected. Strong changes in the amplitude of the gravity anomaly due to a gravity field at higher spatial resolution are not expected based on gravity field data of other bodies¹⁴.

The values for the mascon size and density indicate that it corresponds to mantle material found at shallower depths than expected for isostatic compensation, which we interpret as mantle uplift. This confirms results from a global gravity inversion analysis¹¹. Regions of positive isostatic anomaly due to mantle uplift and other processes are common on the Moon and terrestrial planets at the centres of impact craters¹⁵, and have been suggested to explain the signature at Ceres' largest basin, Kerwan¹⁶. An impact-triggered mantle upwelling can be excluded for that structure, however, because of the lack of large craters (>50 km) or planities interpreted as impact basins¹⁷

with the centre at Ahuna Mons. Instead, the additional mantle material may be indicative of a mantle uplift triggered by a convective plume, as previously suggested¹¹. Whether the convection is solely the expression of hydrothermal circulation in a muddy mantle¹⁸ or was influenced by a large basin very early in the history of Ceres^{11,17} is unclear. The feasibility of convection in the mantle of 400 km radius is tested to first order by estimating the Rayleigh number Ra for an ice–silicate composition with a viscosity of 10^{18} Pa s (for a mixture of ice and antigorite) and further parameters that provide a lower bound on Ra (see methods). Retention of interstitial fluids in the mantle⁷ indicates limited warming of the body up to only a few hundred kelvin, also consistent with the mantle's low density. A key implication is that uplift of the fluid-bearing mantle provides a source of fluids for the formation of Ahuna Mons. The shallowest depth of the mantle beneath the dome, and thus the depth of origin of the fluid, is represented by the top of the mascon, at about 30 km.

A possible but less probable scenario of the mascon solutions ($\sim 225,000$ models) shows independent Gaussian distributions of the mascon parameters compared with the previous configuration (Fig. 3). In this case, the mascon is larger horizontally, and more oblate relative to the previous scenario (Fig. 2a). The mascon centre is deep in the crust, $h=32\pm 1$ km, and is 5 km above the crust–mantle boundary. The density contrast of the mascon to the crust is less determined in this case, with a peak at $\rho_M=1,500\text{--}1,600$ kg m^{-3} . This configuration is interpreted to indicate an isolated, lenticular region within the crust of slightly higher density than the surroundings. The region might have formed by a decrease in porosity due to compaction creep of phyllosilicates if temperatures exceeded 200 K (ref. 13). The regional decrease of the approximately 10 vol.% porosity³ of the crust, however, is insufficient to create the estimated density contrast. Alternatively, the higher density could have resulted from regional filling of the void space of the crust. A likely filling material is aqueous fluids with a few tens of vol.% of suspended hydrated silicate particles ($\sim 2,000$ kg m^{-3}) with densities close to that of the crust. The depth of the lenticular region would represent a buoyancy zone within the crust for most of the aqueous fluids. A fraction of the fluids with slightly lower density might have reached the surface and formed Ahuna Mons. In this case, the representative source point for the Ahuna Mons material is at about 28 km depth, if we assume that it corresponds to the top of the mascon. This scenario inferred from the mascon solutions provides an alternative origin depth for the fluids, although similar to the mantle uplift configuration.

Although it is not possible to distinguish between two possible configurations, we infer very similar values for the depth of origin

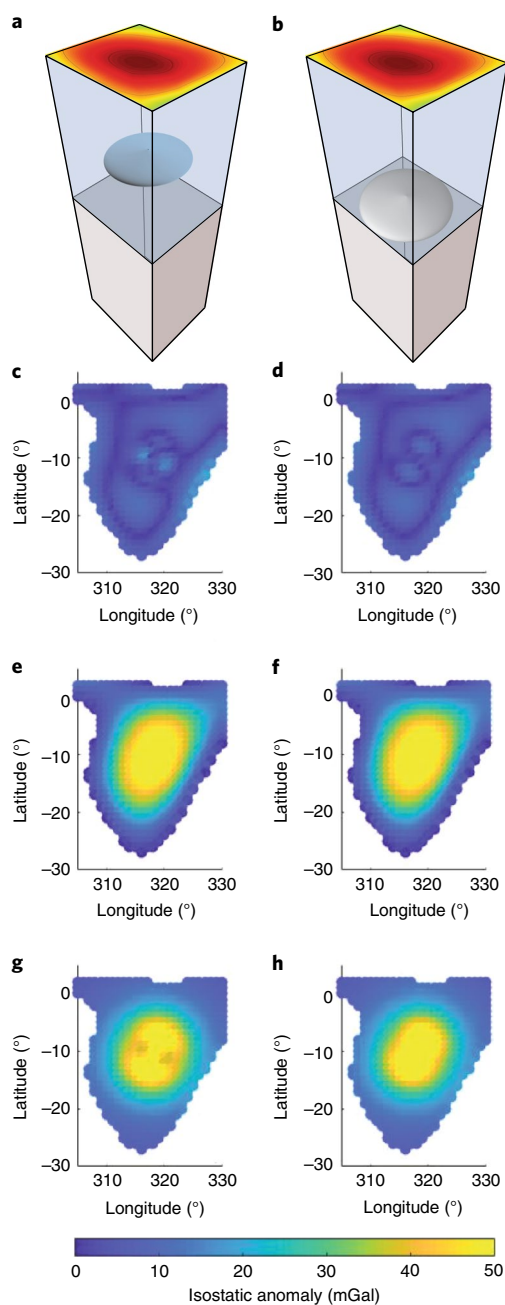


Fig. 2 | Gravity anomaly residuals for two solutions of the mascon analysis. **a, b**, Schematics for the two configurations with an ellipsoidal mascon located in the crust or just above the mantle. **c–h**, Gravity anomaly residuals (**c, d**) between Ceres18C (**e, f**), and two of the solutions of the mascon analysis (**g, h**).

of the fluids producing Ahuna Mons, at a depth of about 30 km. To assess the sensitivity of our solution to the assumed two-layer internal structure, we explored another case with three layers (crust, mantle and core). It is based on a previous study⁴ that suggested the following properties for the layers: a crustal thickness of 33 km and density of $1,400 \text{ kg m}^{-3}$, mantle density of $2,225 \text{ kg m}^{-3}$ and a core 200 km in size and with density $3,410 \text{ kg m}^{-3}$. Assuming these parameters in our MCMC simulations leads to additional results (Supplementary Fig. 6) that are fully in agreement with the solutions based on the two-layer interior model. Although the histograms show two separate Gaussian distributions, the final ensemble for the case based on the three-layer model offers only one scenario

that is consistent with a mantle uplift. That is, both families of solutions yield a mascon located at the core–mantle boundary with a density contrast with the crust of about 800 kg m^{-3} , similar to the difference between mantle and crustal densities. The two families of solutions in the three-layer model provide significant discrepancies only in the horizontal shapes of the mascon.

To evaluate the sensitivity of the results to the use of isostatic anomalies, we tested MCMC simulations using Bouguer anomalies and obtained results similar to those presented above. An alternative approach that uses Bouguer anomalies and a topography anomaly at the crust–mantle interface would only enable us to verify that the strong anomaly is due to a mantle uplift, without the possibility of testing additional mechanisms. The adopted mascon method approach, instead, allows us to consider a variety of different possible scenarios for the cause of the anomaly.

In the following section we are considering the MCMC configuration with the highest probability, that is, the mantle uplift configuration with an inferred depth of fluids of about 30 km.

Slurry extrusion. We now characterize the rheology of a fluid capable of travelling through 30 km of crust while matching the high viscosity inferred from the domical landform of Ahuna Mons⁹. The factor limiting the range of fluid viscosity of a fluid ascending to form domes on Ceres is conductive cooling between the fluid and the vertical conduit wall¹⁹. The temperature of the wall is a function of the Ceres geotherm, estimated at 2.6 K km^{-1} (ref. 19), while the plausible diameter of the conduit throughout the crust is estimated at 10 m on average¹⁹. The initial fluid temperature is set as the minimum eutectic point for pure water (273 K). However, lower temperatures may also be possible if the liquid is a brine, that is, an aqueous solution with dissolved salts²⁰. We use an analytical solution for the conductive cooling¹⁹ to find the minimum velocity that prevents complete freezing of the fluid during ascent to the surface. If complete freezing is achieved, then the fluid behaves as a solid and it is assumed that the flow stops within the crust. With the depth constraint of 30 km, we determined that the ascent velocity must be more than 10^{-5} m s^{-1} . If the fluid is approximated as a Newtonian flow, then the velocity is reached with an initial viscosity lower than 10^8 Pa s . We note that these are limit values and the fluid may have higher velocities that imply lower viscosities. Pure water or brines have sufficiently low viscosity to ascend ($\sim 10^{-2} \text{ Pa s}$), but at extrusion on the surface they exhibit subtle morphologies²¹ that are not compatible with the Dawn observations, whose spatial resolution is sufficient to identify them²². The stiff morphology and high relief of the dome, instead, set a minimum viscosity of at least about 10^3 Pa s during extrusion by analogy with natural and laboratory extrusive constructs^{23,24}. The only plausible material satisfying this constraint is a fluid entrained with about 30–45 vol.% of non-soluble, solid particles, in essence a slurry (Fig. 4).

Colloidal dispersion can exhibit a non-Newtonian behaviour with low apparent viscosity at the relatively high shear rates ($\sim 1 \text{ s}^{-1}$) plausibly experienced during ascent. The slow growth of the dome, instead, occurred in a low-shear-rate regime ($< 10^{-2} \text{ s}^{-1}$), in which case the slurry behaviour is characterized by a viscosity several orders of magnitude higher than at high shear rates and produces morphologies consistent with observations⁹. The transport of non-soluble particles from depth would occur by suspension at the inferred range of ascent velocity and at the low gravity of Ceres²⁵.

A slurry material provides a reasonable explanation for two independent characteristics of Ahuna Mons. Whereas the spectral detection of carbonates on the dome's walls is explained by crystallization of a salt-rich fluid¹⁰, the co-occurrence of the spectral signature of phyllosilicates may correspond to hydrated particles of the parent slurry. From modelling of the viscous relaxation of the dome a composition of about 40 vol.% of non-ice particles mixed with ice was inferred²⁶, a petrology that can be explained by

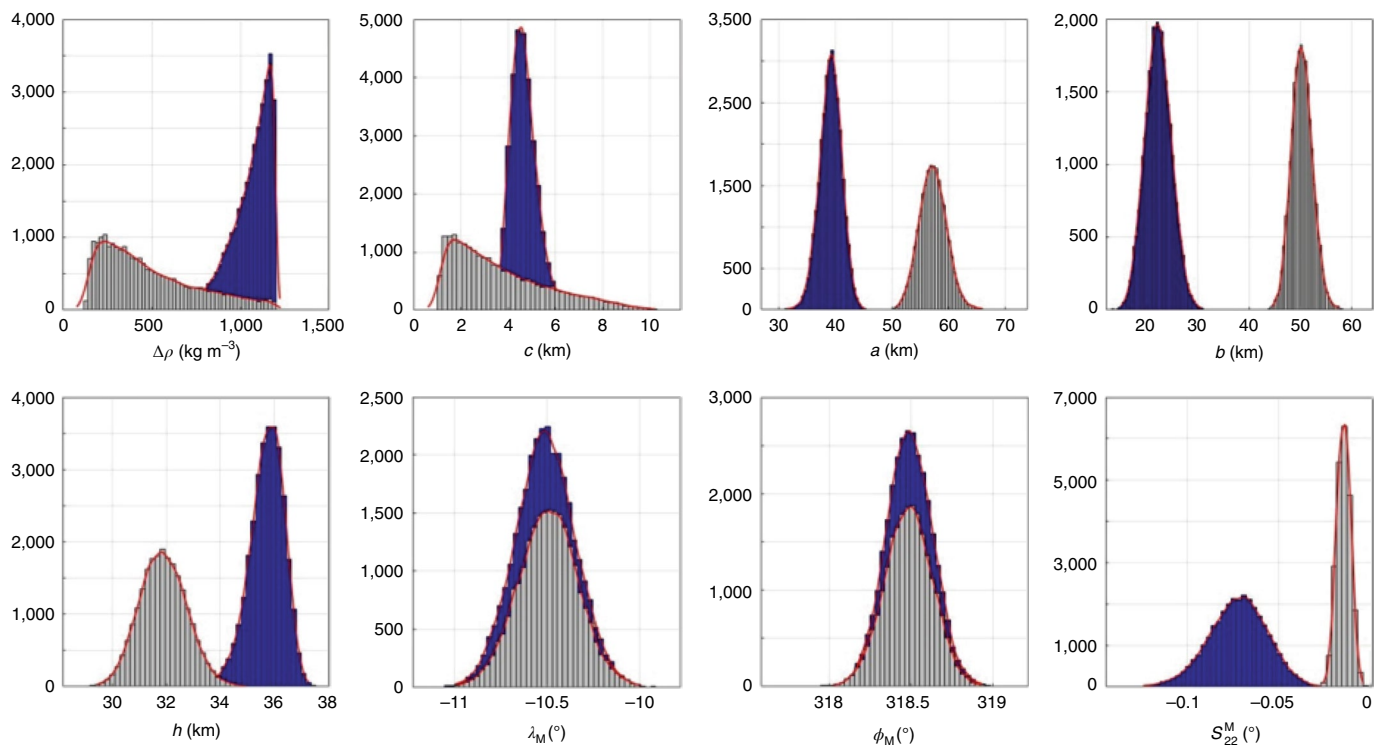


Fig. 3 | Mascon parameters shown as histograms of the final ensemble of solutions. The parameters are $\Delta\rho$, a , b and c ; h , latitude (λ_M), longitude (ϕ_M) and the gravitational parameter S_{22}^M that relies on its horizontal orientation. The histograms are represented by highlighting two scenarios that are consistent with the presence of a mantle uplift (blue) and filling of porosity by fluids (grey).

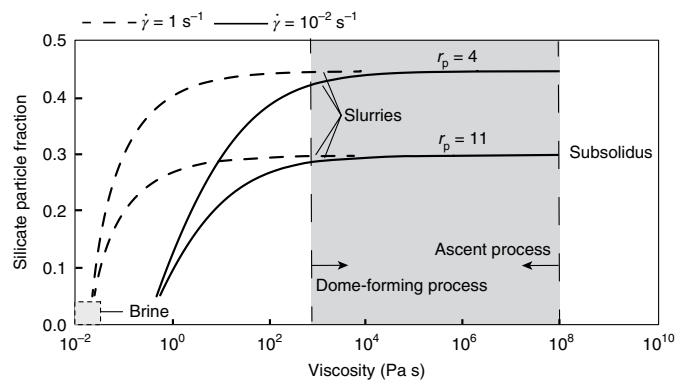


Fig. 4 | Constraints on the properties of the ascending fluid. The solid curves represent the effects of suspended particles on the fluid rheology for particles of aspect ratio r_p (ref. ³¹). For particle fraction higher than about 0.3, the fluids exhibit shear thinning, and the effect of relatively high γ on the apparent viscosity is represented by the dashed curves³². The grey area is defined by the constraints on the lowest viscosity from the dome surface emplacement process and the highest viscosity from the ascent process. For the required viscosities, a relatively high particle fraction is required. A pure brine fluid (dashed square) and a material at subsolidus do not satisfy the constraints.

extrusion and freezing of the proposed slurry. Extrusions of colloidal dispersions have possibly been widespread given the number of domes observed globally²⁷, suggesting that at least a fraction of the minerals detected at the surfaces is of endogenous origin from the deep interior, with a possible contribution from implant from impacts²⁸. Our results support the scenario of a convecting, mud-bearing mantle with efficient heat dissipation, moderate heating

and minor temperature variation^{18,29} for both the early and, given the geologically recent emplacement of Ahuna Mons²⁷, likely current state of Ceres. The properties of Ceres' extrusive material differ from the solid particle-free cryovolcanic fluid³⁰ inferred on icy satellites, and reveals how terrestrial planets, protoplanets and icy moons display extrusive phenomena in a variety of compositional and rheological properties.

Online content

Any methods, additional references, Nature Research reporting summaries, source data, statements of code and data availability and associated accession codes are available at <https://doi.org/10.1038/s41561-019-0378-7>.

Received: 22 October 2018; Accepted: 26 April 2019;
Published online: 10 June 2019

References

1. Russell, C. T. et al. Dawn arrives at Ceres: exploration of a small, volatile-rich world. *Science* **353**, 1008–1010 (2016).
2. Castillo-Rogez, J. C. & McCord, T. B. Ceres' evolution and present state constrained by shape data. *Icarus* **205**, 443–459 (2010).
3. Park, R. S. et al. A partially differentiated interior for (1) Ceres deduced from its gravity field and shape. *Nature* **537**, 515 (2016).
4. Konopliv, A. S. et al. The Ceres gravity field, spin pole, rotation period and orbit from the Dawn radiometric tracking and optical data. *Icarus* **299**, 411–429 (2017).
5. Ermakov, A. I. et al. Constraints on Ceres' internal structure and evolution from its shape and gravity measured by the Dawn spacecraft. *J. Geophys. Res.* **122**, 2267–2293 (2017).
6. Mao, X. & McKinnon, W. B. Faster paleospin and deep-seated uncompensated mass as possible explanations for Ceres' present-day shape and gravity. *Icarus* **299**, 430–442 (2017).
7. Fu, R. R. et al. The interior structure of Ceres as revealed by surface topography. *Earth Planet. Sci. Lett.* **476**, 153–164 (2017).

8. Roatsch, T. et al. DAWN FC2 DERIVED CERES HAMO DTM SPG V1.0, DAWN-A-FC2-5-CERESHAMODTMSPG-V1.0 <https://pds.jpl.nasa.gov/ds-view/pds/viewProfile.jsp?dsid=DAWN-A-FC2-5-CERESHAMODTMSPG-V1.0> (NASA Planetary Data System, 2016).
9. Ruesch, O. et al. Cryovolcanism on Ceres. *Science* **353**, aaf4286 (2016).
10. Zambon, F. et al. Spectral analysis of Ahuna Mons from Dawn mission's visible-infrared spectrometer. *Geophys. Res. Lett.* **44**, 97–104 (2017).
11. Tricarico, P. True polar wander of Ceres due to heterogeneous crustal density. *Nat. Geosci.* **11**, 819–824 (2018).
12. Formisano, M., Federico, C., De Andelis, S., De Sanctis, M. C. & Magni, G. The stability of the crust of the dwarf planet Ceres. *Mon. Not. R. Astron. Soc.* **463**, 520–528 (2016).
13. Neumann, W., Breuer, D. & Spohn, T. Modelling the internal structure of Ceres: coupling of accretion with compaction by creep and implications for the water-rock differentiation. *Astron. Astrophys.* **584**, A117 (2015).
14. Mazarico, E. et al. The gravity field, orientation, and ephemeris of Mercury from MESSENGER observations after three years in orbit. *J. Geophys. Res.* **119**, 2417–2436 (2014).
15. Melosh, H. J. et al. The origin of lunar mascon basins. *Science* **340**, 1552–1555 (2013).
16. Bland, M. T. et al. Morphological indicators of a mascon beneath Ceres' largest crater, Kerwan. *Geophys. Res. Lett.* **45**, 1297–1304 (2018).
17. Marchi, S. et al. The missing large impact craters on Ceres. *Nat. Commun.* **7**, 12257 (2016).
18. Travis, B. J., Bland, P. A., Feldman, W. C. & Sykes, M. V. Hydrothermal dynamics in CM-based model of Ceres. *Meteorit. Planet. Sci.* **53**, 2008–2032 (2018).
19. Quick, L. C. et al. A possible brine reservoir beneath Occator crater: thermal and compositional evolution and the formation of the Vinalia Faculae. *Icarus* **320**, 119–135 (2019).
20. Davis, D. W., Lowenstein, T. K. & Spencer, R. J. Melting behavior of fluid inclusions in laboratory-grown halite crystals in the systems NaCl–H₂O, NaCl–KCl–H₂O, NaCl–MgCl₂–H₂O, and NaCl–CaCl₂–H₂O. *Geochim. Cosmochim. Acta* **54**, 596–601 (1990).
21. Fagents, S. A. Considerations for effusive cryovolcanism on Europa: the post-Galileo perspective. *J. Geophys. Res.* **108**, 5139 (2003).
22. Ruesch, O. et al. Bright carbonate surfaces on Ceres as remnants of salt-rich water fountains. *Icarus* **320**, 39–48 (2019).
23. Blake, S. in *Lava Flows and Domes* (ed. Fink, J. H.) 88–126 (Springer, 1990).
24. Spera, F. J. in *Encyclopedia of Volcanoes* (ed. Sigurdson, H.) 171–190 (Academic, 2000).
25. Shields, A. *Application of Similarity Principles and Turbulence Research to Bed-Load Movement* (Mitteilungen der Preussischen Versuchsanstalt für Wasserbau und Schiffbau, 1936).
26. Sori, M. M. et al. The vanishing cryovolcanoes of Ceres. *Geophys. Res. Lett.* **44**, 1243–1250 (2017).
27. Sori, M. M. et al. Cryovolcanic rates on Ceres revealed by topography. *Nat. Astron.* **2**, 946–950 (2018).
28. Marchi, S. et al. An aqueously altered carbon-rich Ceres. *Nat. Astron.* **3**, 140–145 (2019).
29. Neveu, M. & Desch, S. J. Geochemistry, thermal evolution, and cryovolcanism on Ceres with a muddy ice mantle. *Geophys. Res. Lett.* **42**, 10,197–10,206 (2015).
30. Kargel, J. S. Cryovolcanism on the icy satellites. *Earth Moon Planets* **67**, 101–113 (1995).
31. Krieger, I. M. & Dougherty, T. J. A mechanism for non-newtonian flow in suspensions of rigid spheres. *Trans. Soc. Rheol.* **111**, 137–152 (1959).
32. Sisko, A. W. The flow of lubricating greases. *Ind. Eng. Chem.* **50**, 1789–1792 (1958).

Acknowledgements

The Dawn spacecraft Operations and Flight teams made the observations possible and are acknowledged for their efforts. O.R. is supported by an appointment to the ESA Research Fellow Programme at the European Space and Technology Centre.

Author contributions

O.R. conceived the study and performed the rheology analysis. A.G. developed the mascon model, and performed the gravity and MCMC analyses. W.N. performed the mantle convection analysis. L.C.Q. and J.C.C.-R. contributed to the development of the rheological and compositional concepts. C.A.R., C.T.R. and M.T.Z. contributed to the discussion of the results. O.R. and A.G. wrote the initial manuscript draft. All authors edited the manuscript and approved the final version.

Competing interests

The authors declare no competing interests.

Additional information

Supplementary information is available for this paper at <https://doi.org/10.1038/s41561-019-0378-7>.

Reprints and permissions information is available at www.nature.com/reprints.

Correspondence and requests for materials should be addressed to O.R.

Publisher's note: Springer Nature remains neutral with regard to jurisdictional claims in published maps and institutional affiliations.

© The Author(s), under exclusive licence to Springer Nature Limited 2019

Methods

Bouguer and isostatic gravity anomalies. Dawn's radio science investigation at Ceres enabled the determination of the dwarf planet's gravity field in spherical harmonics to degree (l) and order (m) 18 (ref. ³). This solution, named Ceres18C, is characterized by a spatial resolution of about 82 km (degree 18) at the equator and of about 105 km (degree 14) at the poles. However, the knowledge of $l > 14$ is hampered by the a priori constraint that was assumed in the spherical harmonic framework to estimate Ceres18C (ref. ³). The lower degrees $l < 5$, on the other hand, are dominated by the hydrostatic contribution of the zonal harmonics J_2 and J_4 . Therefore, the range used in this study to yield gravity anomaly maps is $l = 5-14$. This approach permits isolation of the gravity signal that is directly related to subsurface mass anomalies in the area surrounding Ahuna Mons.

A map of the free-air gravity anomalies (g^{FA}) is shown in Supplementary Fig. 1-A. A strong free-air anomaly of about 100 mGal is located in the vicinity of Ahuna Mons. This strong signal accounts for the gravitational contribution of the topography and of the crust-mantle boundary variations associated with isostatic compensation. By subtracting the gravity anomalies predicted by surface topography from the free-air gravity, we determined the Bouguer anomaly map (Supplementary Fig. 1-B). The assumed $\rho_c = 1,287 \text{ kg m}^{-3}$ to compute the gravitational effect of the topography is consistent with the two-layer model in ref. ⁵.

The comparison between gravity and topography, or especially between the measured gravity and gravity expected from topography (g^{T}), allows us to retrieve the gravitational signal associated with relief at the crust-mantle boundary. The admittance (\tilde{Z}) represents a useful tool to provide spectral characterization of gravity and topographic data. If we adopt the gravity derived from topography, we can compute the average admittance per harmonic degree l as follows:

$$\tilde{Z}_l = \frac{S_l^{g^{\text{FA}} g^{\text{T}}}}{S_l^{g^{\text{T}} g^{\text{T}}}}$$

where the power spectral densities $S_l^{g^{\text{FA}} g^{\text{T}}}$ and $S_l^{g^{\text{T}} g^{\text{T}}}$ are given by

$$S_l^{g^{\text{FA}} g^{\text{T}}} = \frac{\sum_{m=0}^l (\bar{C}_{lm} \bar{C}_{lm}^{\text{T}} + \bar{S}_{lm} \bar{S}_{lm}^{\text{T}})}{2l+1}$$

$$S_l^{g^{\text{T}} g^{\text{T}}} = \frac{\sum_{m=0}^l (\bar{C}_{lm}^{\text{T}2} + \bar{S}_{lm}^{\text{T}2})}{2l+1}$$

These expressions rely on the spherical harmonic coefficients of the gravity field Ceres18C (\bar{C}_{lm} and \bar{S}_{lm}) and the gravity derived from topography (\bar{C}_{lm}^{T} and \bar{S}_{lm}^{T}), which is based on Dawn's High Altitude Mapping Orbit (HAMO) stereo photogrammetry (SPG) shape model⁶.

We then computed the isostatic anomalies (g_l^{I}) as the difference between the measured gravity and gravity derived from topography, which is opportunely corrected for the average admittance per harmonic degree, as follows:

$$g_l^{\text{I}} = g_l^{\text{FA}} - \tilde{Z}_l g_l^{\text{T}}$$

The isostatic gravity anomaly map projected on a $482.0 \times 445.9 \text{ km}^2$ ellipsoid is shown in Supplementary Fig. 2. The region surrounding Ahuna Mons has a large isostatic anomaly of about 50–60 mGal. This residual gravity signature provides crucial information on the properties of possible subsurface structures beneath the area that encompasses the cryovolcanic dome.

Three-dimensional ellipsoidal mascon and its gravitational effect. The gravity measurements of Ceres have previously been used to determine the interior structure of the dwarf planet by assuming a global Airy isostatic compensation mechanism⁵. The isostatic gravity anomaly map shows that only a few regions are characterized by substantial residual gravity, which is indicative of local deviation from isostatic compensation. The departure from this state of gravitational equilibrium allows us to study the physical properties of subsurface structures.

A three-dimensional ellipsoidal mascon with uniform density was used to reproduce the gravity signal (Supplementary Fig. 1-B) in the vicinity of Ahuna Mons at $0-20^\circ\text{S}$ and $35-55^\circ\text{W}$. Supplementary Fig. 2 shows the following properties of the mascon: horizontal (a, b) and vertical (c) axes, which correspond to the width and height of the mascon, respectively; $\Delta\rho; h$ or distance from the surface; colatitude (ϑ_M) and longitude (ϕ_M) of the mascon centre; horizontal tilt angle (parameterized as the spherical harmonic coefficient S_{22}^{M} of the gravitational potential of the mascon). These parameters were adjusted in our study to reproduce the observed isostatic gravity anomaly. Preliminary transformation and rotation were required to compute precisely the gravitational acceleration at a generic point P. The isostatic gravity anomalies were retrieved on a sphere with a radius equal to Ceres' mean radius, $R = 470 \text{ km}$. The point P is defined in the planetocentric reference frame (X, Y, Z) with spherical coordinates as $P(R, \vartheta, \phi)$, where ϕ is the longitude ($305-335^\circ$) and ϑ is the colatitude ($90-110^\circ$).

To compute the gravitational potential energy of the mascon, we projected these spherical coordinates in a reference frame with its origin at the centre of the mascon (Supplementary Fig. 3). Therefore, we computed

$$X_P - X_M = \begin{bmatrix} R \cos \phi \sin \vartheta - (R-h) \cos \phi_M \sin \vartheta_M \\ R \sin \phi \sin \vartheta - (R-h) \sin \phi_M \sin \vartheta_M \\ R \cos \vartheta - (R-h) \cos \vartheta_M \end{bmatrix}$$

The resulting vector was, then, reported in the reference frame oriented with the principal axes of the mascon (x_M, y_M, z_M), as follows:

$$x_p = \begin{bmatrix} x \\ y \\ z \end{bmatrix} = R_2(\vartheta_M) R_3(\phi_M) (X_P - X_M)$$

where the rotation matrices $R_2(\vartheta_M)$ and $R_3(\phi_M)$ are defined as

$$R_3(\phi_M) = \begin{bmatrix} \cos \phi_M & \sin \phi_M & 0 \\ -\sin \phi_M & \cos \phi_M & 0 \\ 0 & 0 & 1 \end{bmatrix} R_2(\vartheta_M) = \begin{bmatrix} \cos \vartheta_M & 0 & -\sin \vartheta_M \\ 0 & 1 & 0 \\ \sin \vartheta_M & 0 & \cos \vartheta_M \end{bmatrix}$$

Thus, the gravitational potential energy associated with the density contrast between the mascon and the crust is given by

$$U_M = -\frac{GM_M}{r}$$

$$\left[1 + \left(\frac{R_M}{r} \right)^2 C_{20}^{\text{M}} P_{20}(\cos \vartheta) + \left(\frac{R_M}{r} \right)^2 C_{22}^{\text{M}} P_{22}(\cos \vartheta) \cos 2\phi \right. \quad (S7)$$

$$\left. + \left(\frac{R_M}{r} \right)^2 S_{22}^{\text{M}} P_{22}(\cos \vartheta) \sin 2\phi \right]$$

where R_M is the mean radius of the mascon, which is assumed to be the mean equatorial radius ($R_M = \frac{a+b}{2}$), $r = \sqrt{x^2 + y^2 + z^2}$ is the distance between P and

the mascon centre, $M_M = \frac{4}{3}\pi \Delta\rho abc$ is the incremental mass of the mascon, the unnormalized spherical harmonic coefficients C_{20}^{M} and C_{22}^{M} rely on the size and shape of the mascon as

$$C_{20}^{\text{M}} = \frac{1}{5R^2} \left[(c^2 - a^2) + \frac{1}{2}(a^2 - b^2) \right]$$

$$C_{22}^{\text{M}} = \frac{1}{20R^2} [(a^2 - b^2)]$$

and S_{22}^{M} describes the horizontal tilt angle of the semimajor axes a and b . The associated Legendre and longitudinal functions depend on the relative position of P on the surface, as follows:

$$P_{20}(\cos \vartheta) = \frac{1}{2} [3\cos^2 \vartheta - 1] = \frac{1}{2} \left[\frac{2z^2 - x^2 - y^2}{r} \right]$$

$$P_{22}(\cos \vartheta) = 3(1 - \cos^2 \vartheta) = \frac{3(x^2 - y^2)}{r}$$

$$\sin 2\phi = \left[\frac{2xy}{x^2 + y^2} \right]$$

$$\cos 2\phi = \left[\frac{x^2 - y^2}{x^2 + y^2} \right]$$

The vertical and horizontal geometry between a generic point P and the mascon is shown in Supplementary Fig. 4. We also discretized U_M by using four terms ($U_M = U_{M1} + U_{M2} + U_{M3} + U_{M4}$). The first term is related to the monopole and is given by

$U_{M1} = -\frac{GM_M}{r}$, with G the gravitational constant, and the other three represent the quadrupole terms:

$$U_{M2} = -\frac{GM_M}{r^5} \left[(c^2 - a^2) + \frac{1}{2}(a^2 - b^2) \right] \frac{(2z^2 - x^2 - y^2)}{10}$$

$$U_{M3} = -\frac{3}{20} \frac{GM_M}{r^5} (a^2 - b^2) (x^2 - y^2)$$

$$U_{M4} = -\frac{GM_M}{r^5} 6xy R_M^2 S_{22}^{\text{M}}$$

The resulting gravity anomaly ($|a_M|$) is computed with the gradient in the gravitational potential, as follows:

$$a_M = -\nabla U_M$$

The partial derivatives that are needed to determine the total gravity acceleration are given by

$$\begin{aligned} \frac{\partial U_{M1}}{\partial x} &= \frac{GM_M}{r^3}x \\ \frac{\partial U_{M1}}{\partial y} &= \frac{GM_M}{r^3}y \\ \frac{\partial U_{M1}}{\partial z} &= \frac{GM_M}{r^3}z \\ \frac{\partial U_{M2}}{\partial x} &= \frac{GM_M}{r^7}x \left[(c^2 - a^2) + \frac{1}{2}(a^2 - b^2) \right] \left[\frac{(2z^2 - x^2 - y^2)}{2} + \frac{2}{5}r^2 \right] \\ \frac{\partial U_{M2}}{\partial y} &= \frac{GM_M}{r^7}y \left[(c^2 - a^2) + \frac{1}{2}(a^2 - b^2) \right] \left[\frac{(2z^2 - x^2 - y^2)}{2} + \frac{2}{5}r^2 \right] \\ \frac{\partial U_{M2}}{\partial z} &= \frac{GM_M}{r^7}z \left[(c^2 - a^2) + \frac{1}{2}(a^2 - b^2) \right] \left[\frac{(2z^2 - x^2 - y^2)}{2} - \frac{4}{5}r^2 \right] \\ \frac{\partial U_{M3}}{\partial x} &= \frac{3}{5} \frac{GM_M}{r^7} (a^2 - b^2)x \left[\frac{5}{4}(x^2 - y^2) - \frac{r^2}{2} \right] \\ \frac{\partial U_{M3}}{\partial y} &= \frac{3}{5} \frac{GM_M}{r^7} (a^2 - b^2)y \left[\frac{5}{4}(x^2 - y^2) + \frac{r^2}{2} \right] \\ \frac{\partial U_{M3}}{\partial z} &= \frac{3}{4} \frac{GM_M}{r^7} z (a^2 - b^2) (x^2 - y^2) \\ \frac{\partial U_{M4}}{\partial x} &= \frac{6}{r^7} GM_M R_M^2 S_{22}^M [5x^2y - yr^2] \\ \frac{\partial U_{M4}}{\partial y} &= \frac{6}{r^7} GM_M R_M^2 S_{22}^M [5xy^2 - xr^2] \\ \frac{\partial U_{M4}}{\partial z} &= 30 \frac{GM_M}{r^7} R_M^2 S_{22}^M xyz \end{aligned}$$

The resulting gravity anomaly computed at a generic location $P(x, y, z)$ is given by

$$|a^{\text{com}}| = \sqrt{\left(\frac{\partial U_{M1}}{\partial x} + \frac{\partial U_{M2}}{\partial x} + \frac{\partial U_{M3}}{\partial x} + \frac{\partial U_{M4}}{\partial x} \right)^2 + \left(\frac{\partial U_{M1}}{\partial y} + \frac{\partial U_{M2}}{\partial y} + \frac{\partial U_{M3}}{\partial y} + \frac{\partial U_{M4}}{\partial y} \right)^2 + \left(\frac{\partial U_{M1}}{\partial z} + \frac{\partial U_{M2}}{\partial z} + \frac{\partial U_{M3}}{\partial z} + \frac{\partial U_{M4}}{\partial z} \right)^2}$$

MCMC algorithm. The parameters of the mascon that directly affect the computation of the gravity anomalies are a , b and c ; ϕ_M , θ_M and h ; S_{22}^M and $\Delta\rho$. To sample the multidimensional parameter space, we use the Bayesian inversion approach, which is based on an MCMC algorithm³³. The criterion that is applied to determine the resulting ensemble of models is the minimization of the differences between the local gravity map observed with Ceres18C and that computed with the three-dimensional ellipsoidal mascon. We discretized the local map at 1 degree per pixel (dpp), and we computed the gravity anomalies at each point for both Ceres18C (only with $5 \leq l \leq 14$) and the modelled mascon. The discrepancies between computed and observed gravity anomalies are assumed to have a Gaussian distribution, and therefore the probability function $P(j)$ at each step j used in our algorithm is defined as follows:

$$P(j) = \exp\left\{ \frac{1}{2} \left[(a_1^{\text{com}} - a_1^{\text{obs}}) \dots (a_n^{\text{com}} - a_n^{\text{obs}}) \right] \times \begin{bmatrix} 1/\sigma_g^2 & \dots & 0 \\ \vdots & \ddots & \vdots \\ 0 & \dots & 1/\sigma_g^2 \end{bmatrix} \times \begin{bmatrix} (a_1^{\text{com}} - a_1^{\text{obs}}) \\ \vdots \\ (a_n^{\text{com}} - a_n^{\text{obs}}) \end{bmatrix} \right\}$$

where a_i^{com} and a_i^{obs} are the gravity anomalies at each pixel i computed with the mascon modelling and observed with Ceres18C, respectively. The corresponding standard deviation of each point is assumed to be $\sigma_g = 10$ mGal, which is the accuracy of the gravity field Ceres18C at the equatorial region of the dwarf planet⁴.

The probability distribution of the mascon parameters is mapped using random walkers that are reported in Supplementary Table 1. The parameters are initially selected and then varied randomly with certain boundary conditions. The mascon is constrained to be entirely within the crust. For this reason, we assumed ρ_m as the upper limit of the density of the mascon.

We computed the gravity anomalies of the mascon at each step j , which is the sum of the accepted mascon parameter solution $j-1$ and a random number from a Gaussian distribution multiplied by the random walker step size for each parameter. The solution j is accepted when the ratio $P(j)/P(j-1)$ is larger than a random number generated from a uniform distribution. Otherwise, a new solution is evaluated by always perturbing the previous accepted solution $j-1$ (refs. ^{34,35}).

A proper sampling of the mascon parameters is guaranteed by the use of multiple chains that start from different random initial conditions. The number of chains considered in this study is 40. The convergence of each chain is tested every 10,000 accepted models by computing the mean value and the root mean square (RMS) of the differences between computed and measured gravity anomalies. Once these two values did not change within 10^{-4} mGal, we assumed that the chain had converged. The number of models for each chain is about 200,000, although a few of them converged with about 100,000 or about 400,000 models. These extreme cases, which correspond to three chains, were not considered in our solution. The remaining chains were opportunely mixed to determine the mascon parameters.

The solutions for each chain show an RMS of the gravity residuals of about 6 mGal, which is lower than the accuracy of the gravity field in the equatorial region. However, a certain number of initial models for each chain were excluded because of their larger RMS, which was related to a 'burn-in' period when the solutions were still approaching the target. The mixing of the chains was carried out by selecting every k th model from one of the chains, which is also randomly chosen. This provides a downsampling of the number of models leading to a final number of 50,000 if $k=4$ and the minimum number of models is 200,000.

To test the validity of our results, we also tested other approaches. The probability function that includes gravity anomaly residuals per each pixel (780 points if we consider a 1 dpp map) may overweight these measurements. For this reason, we ran some cases with a probability function with only two parameters: the mean and the RMS of the gravity anomaly residuals. The corresponding standard deviations for the mean and the RMS were 1 mGal and 10 mGal, respectively. The results of these cases did not show notable differences from the solutions presented in this study. Furthermore, we tested different resolutions of the gravity map, in particular 2 dpp and 4 dpp, to be closer to the actual spatial resolution of the gravity field ($\sim 1^\circ$ on the surface), and the resulting parameters of interest were consistent with the case presented in this study with 1 dpp.

Gravity anomaly residuals. The ensemble of solutions that is converged after the MCMC chain mixing shows two possible configurations of the three-dimensional mascon ellipsoid. Both scenarios provide gravity anomalies that are consistent with the isostatic anomaly map of Ceres18C. The gravity anomaly residuals between Ceres18C and the gravity solution of one of the models for each scenario are shown in Fig. 2. The mascon solution on the left is characterized by horizontal semimajor axes $a = 57.9$ km and $b = 50$ km, and a vertical height $c = 7$ km. This mascon is 32 km deep with $\Delta\rho \sim 185$ kg m⁻³. This configuration is consistent with the presence of a brine, and it is representative of the solutions that show a peak at lower density contrast in Fig. 3. Models with $\Delta\rho = 150$ – 400 kg m⁻³ correspond to about 50% of the total number of models for this scenario. The remaining half of these solutions show larger $\Delta\rho$ and c between 1 and 3 km. We also report $\Delta\rho$ as a function of the vertical height of the mascon in Supplementary Fig. 5. Larger values of $\Delta\rho$ (>400 kg m⁻³) in this scenario show small variations of the mascon vertical height, leading to a peak in Fig. 3.

The other solution shown in the right-hand panels of Fig. 2 represents a three-dimensional mascon with $a = 36.4$ km, $b = 19.8$ km and $c = 5.3$ km. The depth of the mascon is closer to the crust–mantle boundary ($h \sim 35.5$ km), and $\Delta\rho \sim 1,070$ kg m⁻³. Since $\rho_M = 2,355$ kg m⁻³ is quite close to the assumed $\rho_m = 2,434$ kg m⁻³ and it is placed at the base of the crust, this family of solutions provides evidence of the presence of a mantle uplift in the surrounding area of Ahuna Mons.

Rayleigh number. For a subcritical Rayleigh number the heat in a system is transferred primarily by conduction, and for a supercritical Ra by convection. For a bottom-heated layer case the Rayleigh number is defined as³⁶

$$Ra = \frac{\alpha g \rho^2 c_p \Delta T_D D^3}{k \eta}$$

with the thermal expansivity α , the acceleration due to gravity g , the density ρ , the heat capacity c_p , the temperature contrast ΔT_D across the reservoir with a thickness D that is tested for convection, the thermal conductivity k and the viscosity η . For a uniformly and internally heated sphere with a rigid outer boundary the Rayleigh number Ra_Q is defined as

$$Ra_Q = \frac{\alpha g \rho^3 c_p Q D^5}{k^2 \eta}$$

with the energy production Q . We used the Dawn estimates¹ for the quantities involved and typical parameter ranges for those that are not constrained further:

- H₂O volume fraction = 10% (a conservative value; a higher water content increases Ra , enhancing convection at low temperatures and consistent with ref. ⁷ and the mantle density composed of water and antigorite)
- $\alpha = 5 \times 10^{-5} \text{ K}^{-1}$
- $g = 0.15 \text{ m s}^{-2}$ (at the mid-depth of the mantle, that is at a radius of approximately 200 km)
- $\rho = 2,400 \text{ kg m}^{-3}$ (the mantle density)
- c_p varying between 700 and 1,080 $\text{J kg}^{-1} \text{ K}^{-1}$ for a temperature of 200–700 K (mass-fraction-weighted arithmetic mean of the H₂O and chondritic heat capacities)^{37–39}
- $\Delta T_D = 10 \text{ K}$ (lower bound)¹³
- $D = 400 \text{ km}$
- k varying between 2.27 and 1.62 $\text{W m}^{-1} \text{ K}^{-1}$ for a temperature of 200–700 K (volume-fraction-weighted arithmetic mean of H₂O and antigorite thermal conductivities)^{40–42}
- η varying between 7×10^{18} and $1.4 \times 10^{12} \text{ Pa s}$ for a temperature of 200–700 K (an average of H₂O ice/water and antigorite viscosities)^{43,44}
- $Q = 0.96H$ where $H = 2 \times 10^{-12} \text{ W kg}^{-1}$ is the present-day energy production by the long-lived radionuclides for an ordinary chondritic initial composition. The scaling of 0.96 takes into account the assumed presence of 10 vol.% of water (that is, 4 wt%).

As a result, for the bottom-heated case, Ra varies between 1.3×10^3 and 1.3×10^{10} in the temperature range of 200–700 K. Supercritical values of $Ra > 3 \times 10^3$ are obtained for $T \geq 230 \text{ K}$.

For the internally driven case, Ra_0 varies between 4.2×10^4 and 6.1×10^{11} in the temperature range of 200–700 K. The supercritical values are between 5.7×10^3 and 3.1×10^4 depending on the convection mode and are obtained for $T \geq 180 \text{ K}$ and $T \geq 210 \text{ K}$, respectively.

Viscosity estimate and particle fraction. To investigate the rheology of a fluid with suspended solid particles (slurry), we considered the model proposed in ref. ³² that describes a Newtonian flow and also accounts for the non-Newtonian effect of shear thinning relevant at a particle fraction ϕ higher than about 0.3 (ref. ⁴⁵). The apparent η at a given γ is³²

$$\eta = \eta_{\infty} + K\gamma^{n-1}$$

where η_{∞} is the apparent viscosity at infinite shear rate, taken here as the viscosity of brine, 10^{-2} Pa s (ref. ⁴⁶). The value for the exponent n describes the shear thinning (pseudo-plastic) for $n < 1$ and is calculated from experimental studies in ref. ⁴⁷ as a function of the particle fraction ϕ . The parameter K is the value of η when $\gamma = 1$ and is calculated using the model presented in ref. ⁴⁸. This latter model assumes the effect of the non-spherical shape of particles⁴⁹:

$$K = \eta_{\phi=0} \left(1 - \frac{\phi}{\phi_m} \right)^{-B\phi_m}$$

where $\eta_{\phi=0}$ is the viscosity for the particle-free fluid, taken as 10^{-2} Pa s (ref. ⁴⁶). The maximum particle packing fraction is ϕ_m and it is inversely proportional to r_p . The parameter ϕ_m and the Einstein coefficient B have been estimated experimentally in ref. ⁵⁰ for particle sizes in the range 25–350 μm . Despite their simplicity, these two models are expected to sufficiently approximate the rheology of the considered material. The lack of further constraints on the particles' properties prevents consideration of additional effects, such as the size distribution (we assume one size only), deformability and aggregation of the particles^{51,52}, as well as the exact temperature of the fluid⁵³.

Data availability

The data Ceres18C described in ref. ⁵ used in this study are available at https://sbn.psi.edu/archive/dawn/grav/DWNCGRS_2_v2/DATA/. The Ceres HAMO Digital Terrain Model described in ref. ⁶ used in this study is available at <https://sbn.psi.edu/pds/resource/dawn/dwnfcshape.html>

Code availability

The computer codes associated with this paper are presented in Methods.

References

- Mosegaard, K. & Tarantola, A. Monte Carlo sampling of solutions to inverse problems. *J. Geophys. Res.* **100**(B7), 12431–12447 (1995).
- Metropolis, N., Rosenbluth, A. W., Rosenbluth, M. N., Teller, A. H. & Teller, E. Equation of state calculations by fast computing machines. *J. Chem. Phys.* **21**, 1087–1092 (1953).
- Hastings, W. K. Monte Carlo sampling methods using Markov chains and their applications. *Biometrika* **57**, 97–109 (1970).
- Schubert, G., Turcotte, D. L. & Olson, P. *Mantle Convection in the Earth and Planets* (Cambridge Univ. Press, 2001).
- Yomogida, K. & Matsui, T. Multiple parent bodies of ordinary chondrites. *Earth Planet. Sci. Lett.* **68**, 34–42 (1984).
- Chase, M. W. Jr *NIST-JANAF Thermochemical Tables* 4th edn (Monograph 9) (National Institute of Standards and Technology, 1998).
- Dorsey, N. E. *Properties of Ordinary Water-Substance in All Its Phases: Water-Vapor, Water, and All the Ices* (ACS Monograph Series 81, Reinhold Publishing Corporation, 1940).
- Ramires, M. L. V. et al. Standard reference data for the thermal conductivity of water. *J. Phys. Chem. Ref. Data* **24**, 1377–1381 (1995).
- Klinger, J. Influence of a phase transition of ice on the heat and mass balance of comets. *Science* **209**, 271–272 (1980).
- Grindrod, P. M. et al. The long-term stability of a possible aqueous ammonium sulfate ocean inside Titan. *Icarus* **197**, 137–151 (2008).
- Shoji, D. & Kurita, K. Compositional diapirism as the origin of the low-albedo terrain and vaporization at mid latitude on Ceres. *J. Geophys. Res.* **119**, 2457–2470 (2014).
- Hilaret, N. et al. High-pressure creep of serpentine, interseismic deformation, and initiation of subduction. *Science* **318**, 1910–1912 (2007).
- Dhodapkar, S., Jacobs, K. & Hu, S. in *Multiphase Flow Handbook* (ed. Crowe, C. T.) Ch. 4 (CRC, 2006).
- Weisbrod, N., Yechieli, Y., Shandalov, S. & Lensky, N. On the viscosity of natural hyper-saline solutions and its importance: the Dead Sea brines. *J. Hydrol.* **532**, 46–51 (2016).
- Turian, R. M., Ma, T. W., Hsu, F. L. G. & Sung, D. J. Characterization, settling, and rheology of concentrated fine particulate mineral slurries. *Powder Technol.* **93**, 219–233 (1997).
- Krieger, I. M. & Dougherty, T. J. A mechanism for non-newtonian flow in suspensions of rigid spheres. *Trans. Soc. Rheol.* **3**, 137–152 (1959).
- Kruif, C. H., van Iersel, E. M. F., Vrij, A. & Russell, W. B. Hard sphere colloidal dispersions: viscosity as a function of shear rate and volume fraction. *J. Chem. Phys.* **83**, 4717–4725 (1985).
- Mueller, S., Llewellyn, E. W. & Mader, H. M. The rheology of suspensions of solid particles. *Proc. R. Soc. A* **466**, 1201–1228 (2010).
- Genovese, D. B. Shear rheology of hard-sphere, dispersed, and aggregated suspensions, and filler-matrix composites. *Adv. Colloid Interface Sci.* **171–172**, 1–16 (2012).
- Tadros, T. F. *Rheology of Dispersions: Principles and Applications* (Wiley-VCH, 2010).
- Darby, R. *Chemical Engineering Fluid Mechanics* (Dekker, 2001).